OPEN ACCESS
IOP Publishing
Superconductor Science and Technology
Supercond. Sci. Technol. **35** (2022) 065019 (15pp)
https://doi.org/10.1088/1361-6668/ac6a85

Systematic study of niobium thermal treatments for superconducting radio frequency cavities employing x-ray photoelectron spectroscopy

A Prudnikava[1,9,*], Y Tamashevich[1,9], S Babenkov[2,10], A Makarova[3], D Smirnov[4], V Aristov[1,2,5], O Molodtsova[2,6], O Kugeler[7], J Viefhaus[1,9] and B Foster[8]

[1] Institute of Experimental Physics, The University of Hamburg, 20148 Hamburg, Germany
[2] Deutsches Elektronen-Synchrotron (DESY), D-22607 Hamburg, Germany
[3] Free University of Berlin, 14195 Berlin, Germany
[4] Technical University of Dresden, 01062 Dresden, Germany
[5] Institute of Solid-State Physics of Russian Academy of Sciences, 142432 Chernogolovka, Russia
[6] ITMO University, 197101 Saint Petersburg, Russia
[7] Helmholtz Centre for Materials and Energy, D-12489 Berlin, Germany
[8] Department of Physics, John Adams Institute, University of Oxford, OX1 3RH Oxford, United Kingdom

E-mail: alena.prudnikava@helmholtz-berlin.de

Received 20 December 2021, revised 1 March 2022
Accepted for publication 26 April 2022
Published 9 May 2022

Abstract

The structural and chemical composition of the surface layer (100–140 nm) of niobium radiofrequency cavities operating at cryogenic temperature has enormous impact on their superconducting characteristics. During the last years, cavities treated with a new thermal processing recipe, so-called nitrogen infusion, have demonstrated an increased efficiency and high accelerating gradients. The role and importance of nitrogen gas has been a topic of many debates. In the present work we employ variable-energy synchrotron x-ray photoelectron spectroscopy (XPS), to study the niobium surface subjected to the following treatments: vacuum annealing at 800 °C, nitrogen infusion, and vacuum heat treatment as for the infusion process but without nitrogen supply. Careful analysis of XPS energy-distribution curves revealed a slightly increased thickness of the native oxide Nb_2O_5 for the infused samples (∼3.8 nm) as compared to the annealed one (∼3.5 nm) which indicates insignificant oxygen incorporation into niobium during 120 °C baking and no effect of nitrogen on the formation of oxides or other niobium phases. By conducting an additional *in-situ* annealing experiment and analyzing the niobium after the failed infusion process, we conclude that the vacuum furnace hygiene particularly during the high-temperature stage is the prerequisite for success of any treatment recipe.

[9] Presented address: Helmholtz Centre for Materials and Energy, D-12489 Berlin, Germany.
[10] Presented address: CEA-Saclay, 91190 Gif-sur-Yvette, France.
[*] Author to whom any correspondence should be addressed.

Supplementary material for this article is available online

Keywords: niobium, nitrogen infusion, superconducting cavity, synchrotron radiation, x-ray photoelectron spectroscopy, niobium oxide, niobium carbide

(Some figures may appear in colour only in the online journal)

1. Introduction

Superconducting radiofrequency (SRF) cavities are the heart of modern accelerators and free-electron lasers—the machines which enable progress in numerous fields of science, medicine and industry. Niobium has become the material of choice for SRF not only due to its superconducting (type-II superconductor, high critical temperature and critical fields) properties, but also due to its ductility, corrosion resistance, high melting temperature etc which makes cavity production by the standard machining and treatment techniques possible. The performance of SRF cavities is characterized by an intrinsic quality factor Q_0 and its dependence on accelerating gradient E_{acc}. A high quality factor of the cavity implies low heat losses and reduction of cryogenic power. Its high value at high field gradients allows the number of accelerating cavities to be reduced while maintaining the same particle energy and cryogenic power. The intrinsic quality factor of the cavity is inversely proportional to the residual resistance of a thin surface layer interacting with the RF field during cavity operation at low temperatures. The interplay between the material parameters (bulk impurity content, grain structure, and cleanliness and smoothness of the inner cavity surface) and the SRF cavity performance has been routinely explored. It was experimentally established that the final low temperature (120 °C) vacuum treatment of a niobium cavity can lead to a significant increase of the quality factor at high field [1]. Even though such a treatment increases residual losses, the total losses are decreased due to lower BCS resistance [2, 3]. There were several studies of material properties to discover the origin of this effect. Among possible explanations are the change of the near-surface dislocation content [4], doping of the niobium surface with vacancy-hydrogen complexes [5, 6], and enrichment [7, 8] or sometimes depletion [9] of oxygen interstitial concentration in the near-surface region. One of the reasons of such a large number of possible causes lies in the difficulty of correlating materials studies with RF properties that can be measured only at low temperature for the entire cavity but not for small niobium samples. Often, cavity cut-outs are studied but this technique is destructive and employs additional machining and exposure of niobium surface to the air and water environment which can alter the surface. Therefore, careful sample preparation is required not to skew the obtained results. After the routine experimental work on cavity thermal processing in the last few years, new processing recipes, nitrogen doping [10, 11] and infusion [12], have been introduced. With these treatments, it was possible to improve the efficiency by up to three times at relatively high accelerating fields. The first treatment [10] consists of niobium surface nitridation at 800 °C (p_{N_2} = 3–5 Pa) with a subsequent nitride removal by electropolishing, which gives a concentration of interstitials within the RF penetration depth. The amount of the material to be removed depends on the duration of the nitridation and usually is between 5 and 10 μm [13, 14]. In a so-called nitrogen infusion recipe, the standard 800 °C/3 h anneal is followed by baking at 120 °C/48 h with N_2 (p_{N_2} = 3–5 Pa) flowing [12]. Thus, as compared to traditional cavity processing, nitrogen gas is added during the final heat treatment and is considered necessary for the improvement of cavity performance characteristics. It should be pointed out that successful infusion has proved hard to achieve by some research institutes [15–17].

By now, several investigations exploring the niobium treated with nitrogen infusion have been published [12, 16–19]. In [12], the pioneering work for nitrogen infusion, secondary electron mass spectroscopy (SIMS) was used to compare the infusion conducted at 120 °C and 160 °C. According SIMS, at 160 °C less Nb_2O_5 and NbO_2 oxides formed, but more carbon and nitrogen reacted with niobium as compared to 120 °C. It was suggested that the infusion step with N_2 supply may decrease the size or amount of carbide precipitates that were observed with the transmission electron microscopy. Additionally exploring the niobium treated with 'argon infusion', the role of carbon and oxygen in niobium (in the absence of nitrogen) for the performance boost of cavities was ruled out.

In [18] the rf performance of single-cell cavities as well as the reference samples infused in the same conditions (120 °C–160 °C) have been investigated. The infusion step at 160 °C showed ∼50% improvement in Q_0 as compared to ∼20% at 120 °C. By scanning electron microscopy (SEM) the surface features have been observed at the niobium infused at 120 °C, 140 °C and 160 °C as compared to 800 °C/3 h treatment. The x-ray photoelectron spectroscopy (XPS) spectra of the niobium infused at 140 °C were interpreted as having oxynitride or nitride bond (though, neither N 1*s*, O 1*s* nor C 1*s* were presented). As to the 120 °C-infusion, SIMS data indicated no clear difference in nitrogen content as compared to the 800 °C/3 h annealing while no XPS data for such treatment was presented. Noteworthy, the carbon content in the near-surface region of niobium upon 800 °C/3 h was negligible as compared to the infused niobium at 120 °C–160 °C.

A detailed study of niobium near-surface composition upon various steps of infusion is presented in [19]. No signs of nitrogen interaction with niobium was observed at 120 °C and below 500 °C by x-ray reflectivity. At 500 °C, the formation of niobium nitride under the oxide layer is confirmed by X-ray reflectivity, X-ray scattering and XPS, but not observed with SEM. One should note that in the mentioned work the niobium

was pre-treated with annealing at 2000 °C/6 h to improve the material crystallinity and purity. Importantly, the infusion process was conducted in a 'static' regime (i.e. N_2 was supplied to reach the required pressure, and then the vacuum pump has been off for 48 h) which is different for the treatment of cavities (both N_2 supply and the pump are on) [19].

An extensive study of the origin of the deteriorated cavity performance upon 120 °C-nitrogen infusion was performed at DESY [17]. The structural changes of niobium surface have been verified both on cavity cut-outs and reference samples treated in the same experiment run. Special attention was paid to investigation of the surface resistance, mean free path and superconducting band gap, local heating, thermal conductivity, as well as trapped flux and their correlation with the carbide formation in cavities.

In order to systematically investigate different surface-treatment methods, it is necessary to obtain detailed information on the chemical state of the cavity surface. In the present work, we employ the method of electron spectroscopy for chemical analysis [20], in particular synchrotron-radiation-excited XPS with variable photon energies to investigate different niobium samples treated with the infusion recipe. With the ability to vary the incident photon energy, it was possible to tune the information depth probed and identify the sequence of various niobium oxidation states with depth as well as improve the fitting model of the spectra, i.e. identify the chemical shifts of niobium bonded to oxygen and carbon within the Nb-3*d* core level with higher precision.

Although currently slightly modified infusion schemes are being tested on cavities [12], we focus our attention on the primary infusion recipe when the nitrogen gas is supplied at 3.3 Pa at 120 °C. We compare the as-treated niobium surface with an identical one also treated at 120 °C but without the N_2 supply (i.e. infusion without nitrogen), as well as a simple 800 °C/3 h anneal in high vacuum, in order to reveal whether nitrogen chemically interacts with niobium. We also compare the as-treated samples with a sample that underwent the treatment together with an SRF cavity at DESY that had demonstrated $Q_0(E_{acc})$ degradation in a subsequent RF test. Additionally, we conducted the *in-situ* annealing of niobium in the preparation chamber of the XPS set-up, which allowed characterization of the surface without an intermediate air exposure and thus free of the native oxide which limits the XPS studies. It will be shown that a prolonged thermal treatment of niobium favors the formation of carbides and nitrides even in ultra-high vacuum (UHV) conditions. These results may explain the differences in chemical composition of niobium treated with the same recipe but in different furnaces. SEM, energy-dispersive X-ray (EDX) analysis, X-ray diffraction (XRD), and Raman spectroscopy complemented the performed XPS studies.

2. Materials and methods

2.1. Sample preparation and thermal treatment procedures

Niobium samples with diameter 1 cm and 2.75 mm height were cut via electrical-discharge machining from a large-grain niobium ingot used in the EXFEL production (manufactured by Heraeus, residual resistivity ratio 550) in a way that each sample represents a single crystal with preferential surface crystal orientation (100) or (110), which was checked with XRD. Prior to thermal treatment, the samples underwent processing in buffered chemical solution ($HF:HNO_3:H_3PO_4 = 1:1:2$) to remove several tens of micrometers from the surface to eliminate contamination from the cutting process, then thoroughly washed in flowing water and rinsed with ethanol.

The vacuum furnace used for the thermal processing of Nb samples consists of a ceramic tubular chamber (diameter 70 mm, 1500 mm length) and operates at a maximal temperature of 1200 °C and at a base pressure of 1×10^{-4} Pa at 800 °C. The temperature during the experiments is controlled by in-built thermocouples in three zones at the outer walls of the ceramic chamber, providing a uniform temperature along the chamber, and with an additional thermocouple located in the vicinity of a sample. A titanium polycrystalline tubular holder covered with a niobium foil was used both as a getter material and a sample support.

In order better to assess the impact of different niobium-processing techniques that have been presented in the literature [12, 18], several thermal-processing recipes were performed in this furnace:

(a) In the first treatment, the samples were annealed at 800 °C during 3 h in vacuum with a background pressure of 3–4 $\times 10^{-4}$ Pa, which is similar to the process vacuum pressure for the thermal treatment of EXFEL cavities, according to the technical specification [21];
(b) For the infusion without nitrogen, the 800 °C anneal period (3 h) was followed by additional 120 °C baking during 48 h in vacuum (7.5×10^{-5} Pa);
(c) For the nitrogen infusion, the 800 °C anneal (3 h) was followed by 120 °C baking in nitrogen gas (99.9999%) supplied at 3.3 Pa for 48 h (the pumping of the furnace was not interrupted during this time). At the end of experiment, the nitrogen supply was terminated and the heating was switched off. The samples were left in vacuum to cool down to room temperature (figure S1, appendix A available online at stacks.iop.org/SUST/35/065019/mmedia).

The Nb(100) samples prepared using recipes (a)–(c) were labelled 'annealed', 'infused without nitrogen', and 'infused', respectively.

One of the samples with the crystal-plane orientation of the top surface close to (110) was subjected to infusion without nitrogen together with a single-cell SRF Nb cavity in another, significantly larger furnace at DESY. The details of the experimental procedure are described in [16, 17]. It should be noted that the base pressure, at the time when the corresponding temperature of the annealing process was reached, was measured close to the pump and was of the same order as in the procedures described above. The cavity demonstrated deteriorated performance characteristics (both the efficiency and maximal accelerating-field gradients) after this treatment. All the samples described above were extracted from the furnace

and were kept for several days in air environment prior to characterization.

To complement our investigation, we annealed a Nb(110) sample in UHV (950 °C/2 × 10^{-6}–2.5 × 10^{-7} Pa/11 h) in the preparation chamber of the XPS set-up at the Russian-German Beamline (RGBL) at BESSY II [22]. The sample heating was performed via electron bombardment produced by thermal emission from a tungsten filament located at the bottom of the sample. To reach the required temperature, a biasing voltage of 0.5–1 kV was additionally applied for electron acceleration. The sample was studied immediately after the annealing after it was cooled to room temperature in UHV without intermediate air exposure.

2.2. Sample characterization with XPS and fitting procedure of Nb 3d core level

The investigation of the chemical composition of the samples subjected to the ambient environment was performed using synchrotron-radiation-excited XPS at an end-station based on an Argus photoelectron analyzer with a 128-channel high-sensitivity detector, integrated in the P04 beamline at PETRA III (DESY, Hamburg) [23, 24]. The overall resolution of the experimental setup was 30 meV. The spectra were collected in the range of incident-photon beam energies of 800–1500 eV and at an angle close to normal emission (72°). The excitation-energy range was chosen as a compromise between the maximum sensitivity of the detector and the optimal escape depth. The narrow-band high-resolution photoemission-energy distribution curves (EDCs) were collected with a constant pass energy of 10 eV. The sample annealed *in-situ* was measured at the dipole RGBL, BESSY II synchrotron-radiation facility (HZB, Berlin) at photon-beam energies of 450–1000 eV and normal-emission geometry at a 55° angle between the incident beam and the analyzer aperture. The binding-energy (BE) scale of the spectra measured at both facilities was calibrated using the Au-4$f_{7/2}$ core-level peak located at 84.0 eV measured at a metal foil. The spectra were analyzed using the CasaXPS software package. The EDCs of interest in the present work included Nb 3*p*, O 1*s*, C 1*s*, N 1*s*, and in some cases Ti 2*p*, with the main focus on Nb-3*d* core-level region.

The niobium chemical state was determined via systematic analysis of the Nb-3*d* core level. The spectrum-fitting procedure of the samples subjected to the ambient environment was performed as follows. The background was modelled with an Iterated Shirley-type with offsets [25]. In the fitting model we considered the binding-energy shifts (ΔBE) of niobium oxides found in the literature and the NIST XPS Database [26]. A well-known linear dependence of the ΔBE of niobium oxides versus niobium valence was considered as a starting point [27, 28]. The core-level peak features were decomposed as doublets with a constant spin-orbital splitting of 2.75 eV and branching ratio $3d_{5/2}/3d_{3/2}$ of 1.5. The Nb compounds having metallic conductivity including pure niobium Nb^0, interstitials ($Nb^{+0.4}$ and $Nb^{+0.6}$), oxides (Nb^{+1}, Nb^{+2}, and Nb^{+3}) and carbides were fitted with the standard CasaXPS lineshape representing a numerical convolution of a Lorentzian with a Gaussian function with asymmetry, LA(1.2,5,12), while

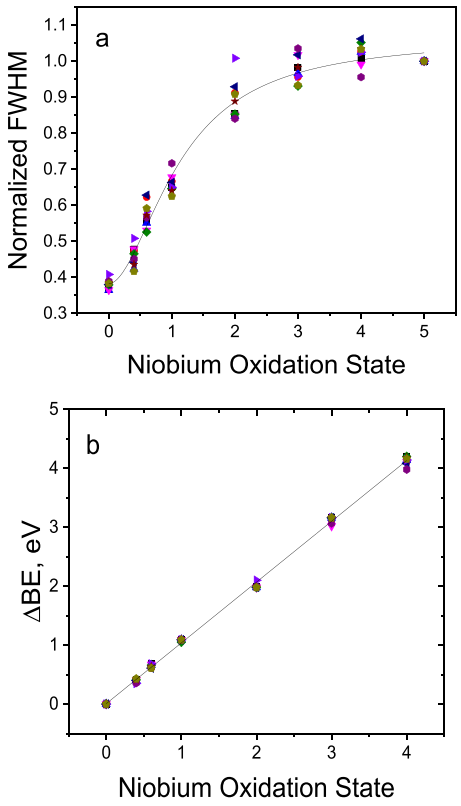

Figure 1. (a) Fitting of the FWHMs with a logistic-function $y = a_2 + (a_1 - a_2)\,(1 + x/x_0)^p$, where x is the niobium oxidation state; (b) linear fit of the binding energy shift, ΔBE, of the fitted components within Nb $3d_{5/2}$ core level as a function of Nb oxidation state. The error bars are smaller than the symbol size.

the oxides with semiconducting- or dielectric-conductivity type ($Nb^{+5,}$ Nb^{+4}) were fitted with a symmetric lineshape LF(1,1,25 280) [29]. A detailed description of these lineshapes can be found in the work of Major *et al* [30]. The fitting process of the full widths at half maximums (FWHMs) of doublets was iterative. Firstly, FWHMs were obtained by fitting the spectra without the FWHM constraints. Then, these values were approximated with a logistic-function (figure 1(a)). Finally, the fitting model was updated with the obtained FWHMs, and the BE shifts were optimized with respect to the minimal residual χ^2 (figure 1(b)). The obtained FWHMs and BEs of the Nb compounds are presented in table 1.

Analysis of the XPS spectra of the *in-situ* annealed sample was performed using the ΔBE for the oxide and carbide components obtained by the routine described above and the literature data. The ΔBEs of the nitride components obtained in our recent XPS study of the nitrided niobium surface were used, which will be published elsewhere. Within Nb 3*d*, the LA(1.2,5,12) lineshape was chosen for the doublet components of niobium compounds, while LA(0.9, 1.8, 12) was used for the metallic niobium Nb^0.

The samples were additionally characterized by SEM (FEI Nova NanoSEM 450 and Zeiss Merlin equipped with an Energy-Dispersive Analyzer (Ultim Extreme, Oxford Instruments). Furthermore, XRD measurements were performed with the Bruker D8 Advance system employing a Cu K_α

Table 1. Binding energy shifts with respect to Nb^0, ΔBE, and the full width at half-maximums (FWHMs) of the fitted components of Nb 3*d* core level obtained for the annealed, infused and infused without N_2 niobium.

Oxidation state	Nb^{+5}	Nb^{+4}	Nb^{+3}	Nb^{+2}	Nb^{+1}	$Nb^{+0.6}$	$Nb^{+0.4}$	Nb^0
BE shift (eV)	5.66 ± 0.005	4.13 ± 0.115	3.14 ± 0.09	1.99 ± 0.05	1.087 ± 0.035	0.64 ± 0.04	0.39 ± 0.03	201.94 ± 0.07 (BE)
FWHM (eV)	1.163 ± 0.070	1.188 ± 0.160	1.137 ± 0.090	1.035 ± 0.260	0.766 ± 0.060	0.666 ± 0.100	0.532 ± 0.110	0.443 ± 0.07

anode. The XRD patterns were measured both in Bragg–Brentano focusing geometry (2Θ/ω scans) as well as at various angles ω of incident photon beam (Small-Angle x-ray Scattering, SAXS) corresponding to scattering depth in the range 40–400 nm for pure Nb.

3. Results

3.1. Niobium upon 800 °C anneal, infusion, and infusion without N_2 supply

Inspection of the treated niobium samples with SEM in secondary electron mode did not reveal any surface changes as compared to the untreated surface (figure S2, appendix A). This observation is different from [18] where the surface features have been observed at the niobium infused at 120 °C as compared to 800 °C/3 h treatment. This possibly can be explained by the fact that in the mentioned work observation was performed with back-scattered electrons providing information from higher depths as well as the elemental contrast.

The low-resolution EDCs (pass energy 50 eV) collected from the annealed Nb at 800 °C and the infused with or without nitrogen taken at $h\nu = 1000$ eV are presented in figure 2. The spectra look similar and are dominated by Nb-3*d*, Nb-3*p* O-1*s*, C-1*s* core-level transitions. The O *KLL* Auger lines are also visible. The niobium subjected to the infusion recipe contains distinct peaks within the Ti-2*p* region, unlike the other treatments. Unlike the results of [18] in which the infused niobium samples demonstrated carbon enrichment in the near-surface layer as compared to the 800 °C-annealed niobium, the carbon content is similar for all the samples described here (figure 2, appendix A, table S1).

As an example, the typical high-resolution EDCs ($h\nu = 1200$ eV) for the regions of interest of the infused sample are shown in figures 3(a)–(d). The spectra represent unaltered experimental data with the fitted Shirley background and chemical-state components.

In figure 3(a), N-1*s* together with Nb-3*p* regions are shown together to compare intensities. A broad peak above 400 eV (figure 3(a), inset) originates from the organic nitrogen-containing species adsorbed at the surface inhomogeneities after exposure to the ambient environment. A broad feature below 400 eV is observed in all the spectra collected at $h\nu = 1000$–1500 eV but not at 800 eV, which may originate from a small amount of nitrogen bonded to niobium. Since this feature is not clearly resolved, the Nb nitrides were not considered in the fitting model of Nb 3*d* of the samples prepared with recipes I–III, but it was taken into account during the data interpretation.

The C-1*s* core level is represented by carbonaceous adsorbate commonly found at the surfaces of solids after exposure to air and is often called adventitious carbon (figure 3(b)). It has been fitted with four contributions. The most intense is located at 285.3 eV and is interpreted as the non-graphitic C–C and C–H bonds.

O 1*s* is well fitted with three contributions: 530.6, 531.5 and 532.7 eV (figure 3(c)). The first is associated with O^{-2} ions in niobium oxides. The second peak is assigned to low-coordination-number O^{-1} ions that are compensating for some deficiencies in the oxide subsurface [31]. The feature at 532.7 eV is assigned to weakly adsorbed species such as aliphatic C–O–C, etc [32]. A fourth component at 530.2 eV was added to account for Ti oxides present in trace amounts in this sample.

The Ti-2p core region (figure 3(d)) shown is specific and maximal for the infused niobium (figure 2). It is found in the form of the Ti^{+4} oxidation state, corresponding to TiO_2 (88.5%) with some contribution of Ti^{+3}, most evidently Ti_2O_3 (11.5%). To estimate the amount of Ti contamination, an approximate estimate of sample near-surface composition was performed and is presented in table S1 (appendix A). The data were obtained by correcting the total component area per photoionization cross section of a respective atomic orbital and inelastic mean free path (IMFP) of photoelectrons approximated as $\lambda \propto {E_{\mathrm{kin}}}^{0.71}$ and therefore may have substantial error. The angular distribution of the photoelectrons was not considered. Thus, according to the presented data, the annealed sample and that infused without nitrogen contain up to four times less Ti species (0 and 0.58 vs. 2.39 at%) at the surface. This suggests that nitrogen may act as a carrier-gas for the vaporized titanium. The origin of titanium in the vacuum chamber is the tubular titanium holder used as a getter material in the vacuum furnace during the thermal processing. Evidently, the titanium vapor is created in the chamber during the preceding 800 °C step, and during the 120 °C-baking period, the nitrogen flow in the vacuum chamber promotes surface contamination of the treated metal. Evidently, it gets oxidized subsequently when the samples are exposed to air.

The presented analysis of the spectra leads to the conclusion that there is no distinguishable difference between any of the samples in terms of the formation of niobium nitride or carbide phases in the experimental conditions under investigation. The absence of these phases at the niobium surface

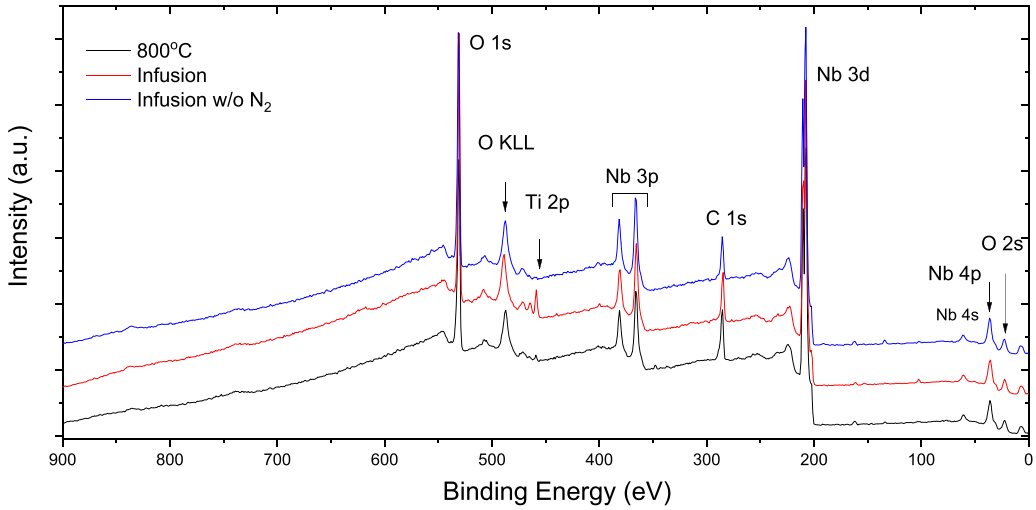

Figure 2. (a) Wide-range EDCs of the 800 °C-annealed, infused and infused without N_2 niobium collected at $h\nu = 1000$ eV.

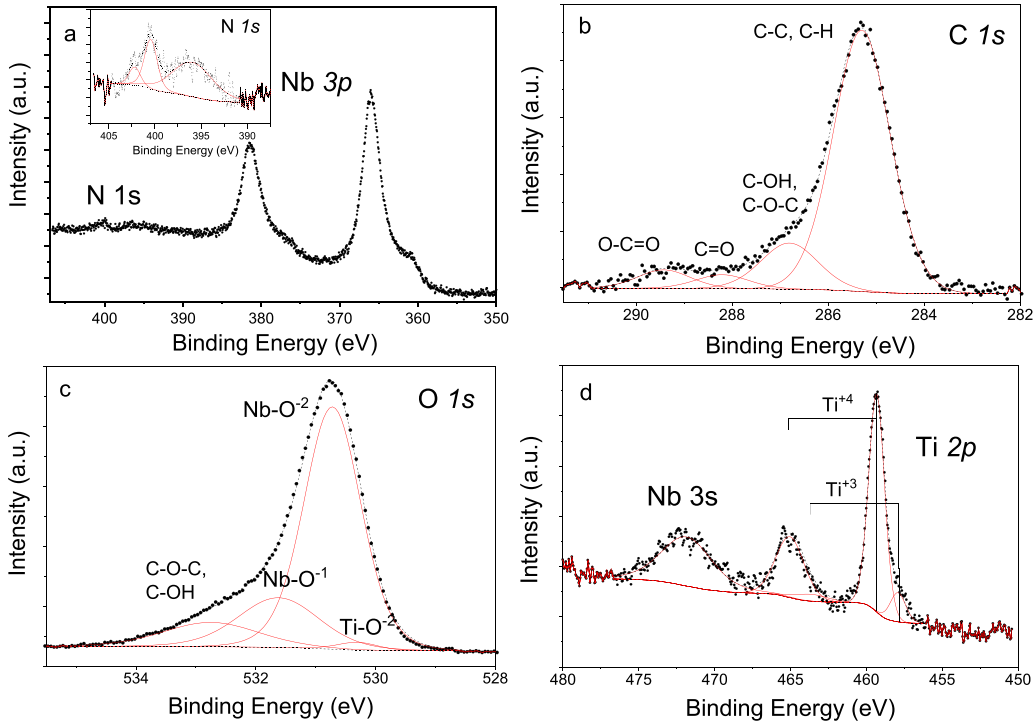

Figure 3. High-resolution EDCs of the infused niobium collected at $h\nu = 1200$ eV: Nb 3*p* (a), C 1*s* (b), O 1*s* (c), and Ti 2*p* (c). Inset in figure (a) shows a magnified N 1*s* core level with fitted components (see description in the text).

subjected to 120 °C-infusion treatment agrees with the data of [19].

The Nb-3*d* core-level spectra, background subtracted and normalized to the maximum peak intensity and taken at various photon energies, are presented in figure 4(a). The higher the photon energy, the larger the average depth probed and therefore the more intense are the contributions from the sample bulk. To determine the Nb chemical state, all the spectra along with a metallic Nb^0 doublet were fitted with five doublets corresponding to niobium oxides with various oxidation states ranging from +5 to +1. Additionally, contributions from oxygen interstitials in octahedral positions within the niobium crystal lattice were included in the model as $Nb^{+0.6}$ and $Nb^{+0.4}$. Peak positions, as well as the respective FWHMs estimated by the procedure described in section 2.2 are summarized in table 1. An example of the measured Nb-3*d* spectrum with the fitted components of the infused sample collected at $h\nu = 1200$ eV is presented in figure 4(b). The relative percentage areas of the fitted peaks are summarized in table S2 (appendix A). Generally, as the photon energy rises, the relative intensity of the higher-valence contribution Nb^{+5} decreases, which confirms that the Nb^{+5} (Nb_2O_5) is the uppermost surface layer. The data imply that the relative contribution of the Nb^{+5} is

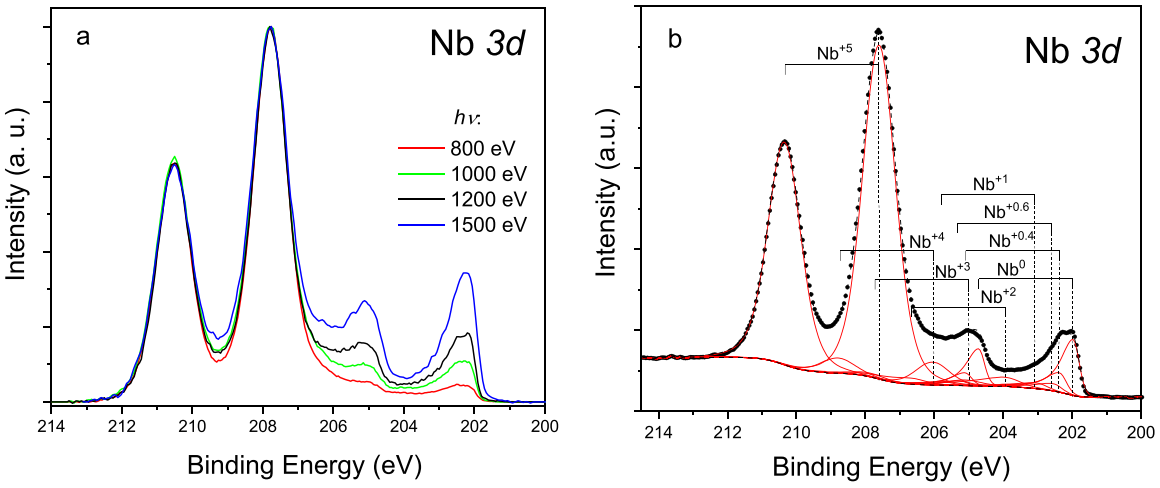

Figure 4. (a) High-resolution EDCs of Nb 3*d* region of the infused niobium collected at $h\nu = 800$, 1000, 1200 and 1500 eV. The spectra are unaltered experimental EDCs with a subtracted Shirley background and normalized to the maximal peak intensity, for reasons of comparison only. (b) An example of the fitted Nb 3*d* region ($h\nu = 1200$ eV).

Table 2. The calculated IMFPs of the photoelectrons originating from the Nb 3*d* region (with respective kinetic energy depending on the incident photon energies) for pure niobium and its compounds according to G1 equation[a] [33].

$h\nu$ (eV)	λ_{Nb} (nm)	$\lambda_{Nb_2O_5}$ (nm)	λ_{NbO_2} (nm)	$\lambda_{Nb_2O_3}$ (nm)	λ_{NbO} (nm)
800	1.35	1.63	1.34	1.12	1.24
1000	1.65	2.01	1.65	1.38	1.52
1200	1.95	2.38	1.95	1.63	1.80
1500	2.37	2.90	2.38	1.98	2.19

[a] The bulk density of the compounds ρ (g cm^{-3}) used in the calculation is the following: Nb: 8.57, NbO: 7.3, NbO_2: 5.9, Nb_2O_3: 7.5, Nb_2O_5: 4.6, Nb_2N: 8.08.

smallest in the annealed sample compared to either of the infused ones.

Assuming the elastic-scattering effects are negligible and attenuation of the electron flux is exponential in the direction normal to the sample surface, the thickness of the uppermost oxide layer (Nb_2O_5), d, can be estimated using the following relationship:

$$\frac{S_l}{S_s} = \frac{\lambda_l \rho_l}{\lambda_s \rho_{ls}} \frac{1 - \exp\left(-\frac{d}{\lambda_l \sin\theta}\right)}{\exp\left(-\frac{d}{\lambda_l \sin\theta}\right)}, \qquad (1)$$

where S_l and S_s are the areas of the overlayer and substrate photoelectron peaks, respectively, ρ_l, ρ_s are the respective atomic densities in g cm^{-3}; λ_l, λ_s are the IMFPs of the appropriate photoelectrons and θ is the photoelectron emission angle with respect to the sample surface [34–36].

The IMFPs of niobium and its compounds were calculated using a universal predictive equation for the IMFPs of X-ray photoelectrons and Auger electrons (G1 equation) described by Gries [33]. The obtained IMFPs of niobium within the photoelectron kinetic-energy range of 600–1300 eV (table 2) are in good agreement with the values predicted later by Tanuma *et al* [37] As the obtained IMFP values of NbO_2 and NbO are comparable to the IMFP of Nb, in the present two-layer model the pentoxide was considered as an overlayer, while the remaining niobium compounds along with the pure metal were considered as 'a substrate' in our calculation. This assumption is supported by the value of the fit residual compared to the case when all oxides are assumed to be an overlayer.

The fitted thickness of Nb_2O_5 is slightly lower for the annealed sample and is equal to ∼3.5 nm as compared to ∼3.8 nm in the samples processed with either infusion recipe (figure 5). Evidently, niobium is still reacting with oxygen present in the chamber during the 120 °C/48 h-infusion step; this process is unaffected by the addition of gaseous N_2.

Despite a visual similarity of the collected spectra, a detailed analysis of the oxides distribution within the probed information depth shows that a small difference (within 1%-peak area) exists. In figure 6 the relative peak areas of the fitted components within the Nb-3*d* core level are plotted against the 90%-information depth (the depth normal to the surface from which 90% of the detected signal originates [20]) for the three samples. A clear difference is observed for the annealed niobium. It has less Nb^{+3}, but more Nb^{+2} and Nb^0 compared to the infused sample. As to the samples infused with and without N_2, some differences are observed for higher photon energies, i.e. as the information depth increases. Particularly for the infused niobium, less Nb^{+4} and Nb^{+2} and more Nb^{+3} is found compared to the niobium infused without N_2. The

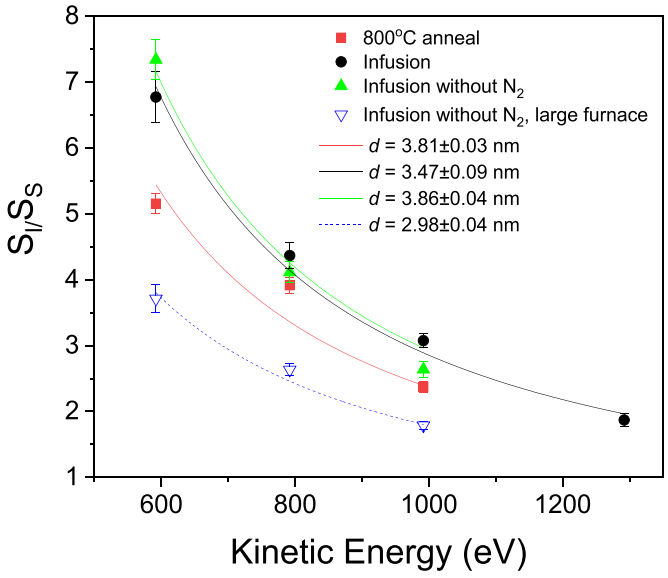

Figure 5. S_I/S_s ratio plotted as a function of photoelectron kinetic energy. Symbols represent the experimental data. The curves show the simulated Nb_2O_5 thickness, d, nm, according to (equation (1)) for the following treatments: 800 °C anneal (red squares), infusion (black circles), and infusion without nitrogen (green triangles). The data for the infused without nitrogen niobium treated in a large furnace simultaneously with the single-cell 1.3 GHz cavity at DESY (blue down-pointed triangles) are shown for comparison. For details see section 3.3.

latter also has the lowest percentage of $Nb^{+0.6}$. The observed dependence has to be explored further by gaining more statistics on thermal-processing experiments, as well as exploration by other techniques. It is important to note that there could be other interstitials along with oxygen atoms, such as N or C, at positions $Nb^{+0.6}$ and $Nb^{+0.4}$ which have not been clearly resolved within N-1*s* or C-1*s* core levels owing to the presence of Nb_2O_5 oxide at the sample surface. Thus, for more accurate analysis of the interstitial content, an *in-situ* XPS experiment would be more appropriate, since it would be free from the native oxide layer suppressing the signal from the region of interest.

3.2. Niobium upon infusion without N_2 with a 1.3 GHz cavity at DESY

The SEM images of the Nb sample treated in the larger furnace together with a single-cell Nb cavity (1DE17) are shown in figure 7. The image in figure 7(a) obtained in a secondary-electron mode demonstrates the submicrometer-size pyramid-shape precipitates which can presumably be assigned to a niobium-carbide phase. The image obtained in a back-scattered electron mode additionally reveals the elongated surface features (figure 7(b)) which could be assigned to the same or another carbide phase or even oxides. To gain more information on the nature of these precipitates, EDX elemental mapping was performed at a decreased accelerating voltage of incident electrons (2 kV), below the threshold for x-ray emission for niobium (Nb $L\alpha$ line) in order to enhance the surface sensitivity and the sensitivity to light elements (figure 8(a)). This revealed that the enrichment of carbon occurs both at the location of the pyramid-shape precipitates and the elongated features, while the surrounding area is heavily enriched with oxygen (figures 8(b)–(f)).

The XRD patterns revealed the reflections arising from Nb(110), (211) and (220) crystal planes from the bulk Nb (figure 9). The other reflections (33.29°, 36.08°, 58.83°, 110.81°) belong to Nb surface compounds. Although these data seem to be ambiguous, based on SEM/EDX analysis above it seems plausible that the reflections can be assigned to niobium carbide. The best matching was attained with the orthorhombic α-Nb_2C (*pnam*) having lattice parameters $a = 10.92$ Å, $b = 4.974$ Å, $c = 3.09$ Å (PDF 04–015-4936). Moreover, the identified crystal planes (201) and (020) in space are closely related to the orientation of precipitates in the SEM images (figures 7(b) and 8(a)–(c)). The α-Nb_2C phase (*pbcn*, $a = c = 4.956$ Å, $b = 0.624$ Å) is an alternative interpretation of the pattern, but worse matching was obtained for the 33.29 ° and 110.8° reflections, so the former was preferred in figure 9. The formation of α-Nb_2C in such thermal conditions agrees with recent findings [38], despite the presence of the excess oxygen, which might have had an impact on the final phase formation. No satisfactory agreement of the XRD pattern was observed with any other known hexagonal or trigonal semicarbides or any oxide phases.

The EDCs of Nb 3*d* as a function of photon energy taken from this sample are presented in figure 10(a). As for the other samples under investigation, the relative intensities of the Nb^{+5} doublets were found to be more intense for the higher photon energies because of the higher surface sensitivity. Fitting of the spectra was performed as described earlier, but with an additional doublet having ΔBE(FWHM) of 0.94 ± 0.01(0.62 ± 0.02) eV (figure 10(b)). As the C-1*s* level revealed a clear peak at ∼382.3 eV (figure 10(c)), the doublet was identified as originating from Nb–C bonds. The existence of more types of carbide bonds was also considered, but such an approach did not result in any improvement of the fit. The N-1*s* region demonstrated a weak peak at 400 eV associated with the adsorbed nitrogen species, as well as a broad peak at 395.1 eV which may arise from Nb–N bonding, similar to previously described samples (figure 3(a)). The fitted FWHMs and ΔBE, as well as the percentage area of the Nb-3*d* core level, are summarized in tables S3 and S4 (appendix A). As compared to the other thermally treated samples, the fitting of Nb 3*d* resulted in a smaller relative contribution of Nb^{+5}, Nb^{+4} and Nb^{+3}, but higher Nb^{+2}. Another important difference is the depletion of the $Nb^{+0.4}$ contribution (figure 6). The calculated pentoxide thickness according to equation (1) was the smallest among all the samples in this study (2.88 ± 0.08 nm), which can be explained by the reduction properties of carbon favoring the formation of oxides with lower oxidation states [39] and/or a discontinuous Nb_2O_5 layer.

These considerations lead to the conclusion that the degradation of the cavity performance was caused by the niobium carbide (Nb_2C), as well as the surrounding area that is heavily enriched with oxygen (predominantly NbO), formed during the infusion process conducted in the large furnace.

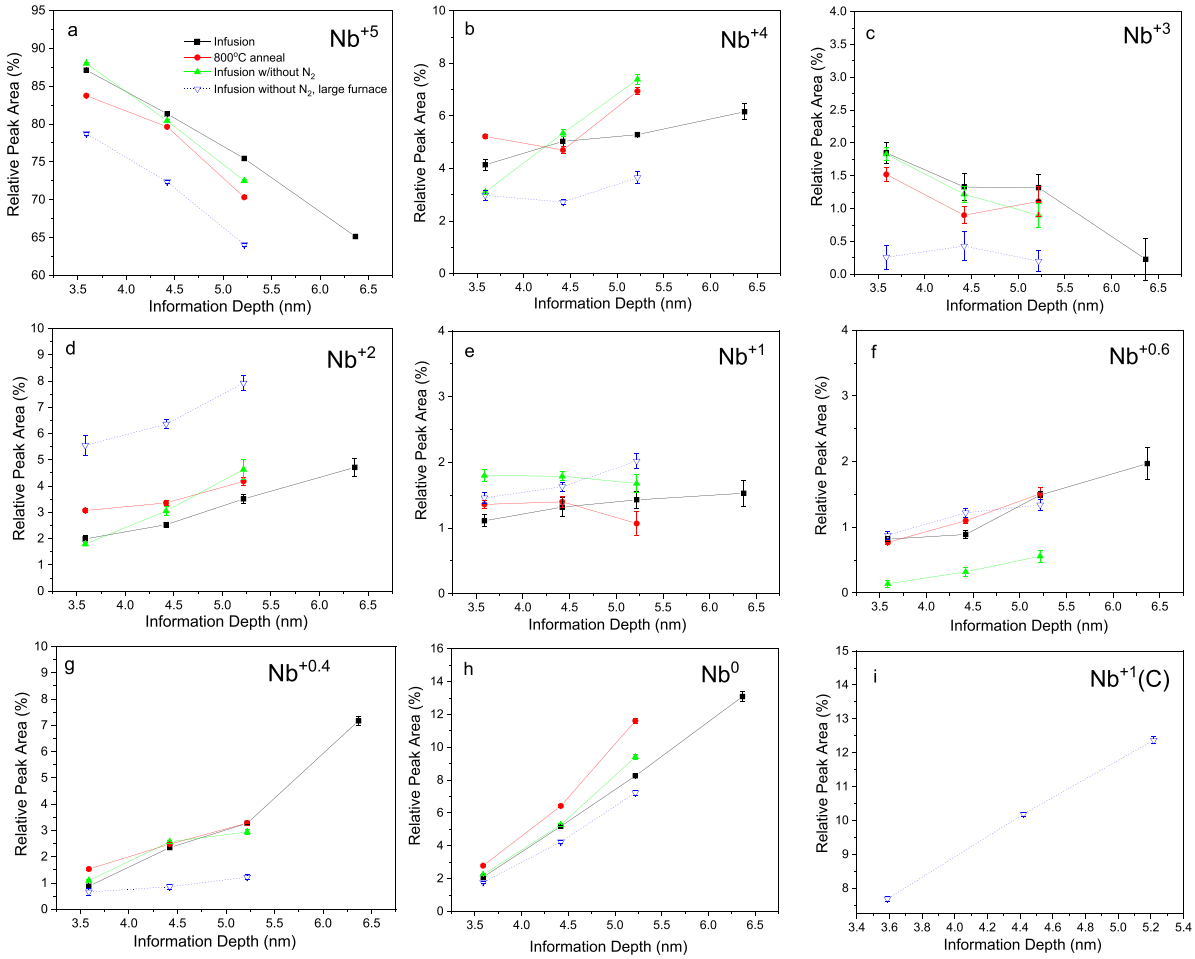

Figure 6. Relative peak areas of Nb 3*d* doublets representing niobium in various chemical states upon vacuum anneal at 800 °C (red squares), infusion (black circles) and infusion without N_2 (green triangles): (a) Nb^{+5}, (b) Nb^{+4}, (c) Nb^{+3}, (d) Nb^{+2}, (e) Nb^{+1}, (f) $Nb^{+0.6}$, (g) $Nb^{+0.4}$, (h) Nb^{0}, (i) Nb^{+1}(C). The data for the niobium infused without nitrogen treated in a large furnace simultaneously with the single-cell 1.3 GHz cavity at DESY (blue down-pointing triangles) are shown for comparison. For details see section 3.3. The data are plotted for several photon energies corresponding to different information depths (*x*-axis).

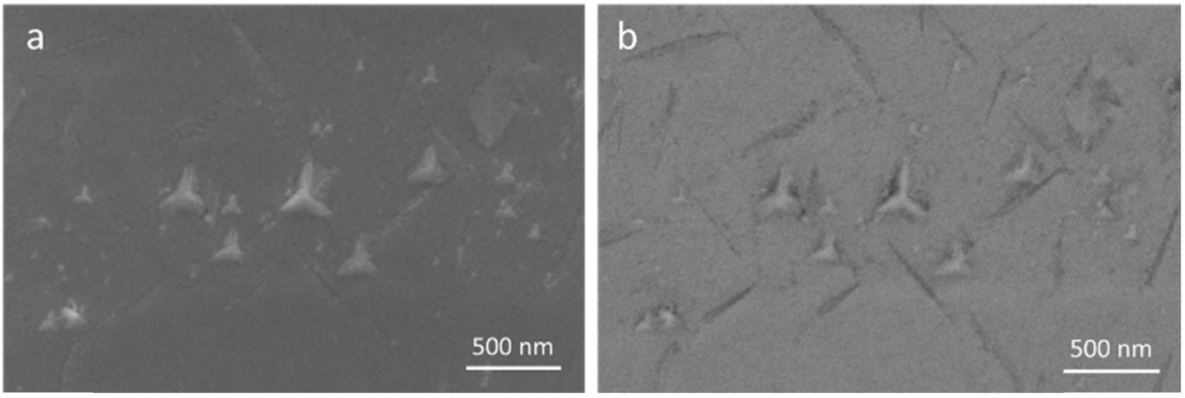

Figure 7. SEM images of Nb sample infused without N_2 together with a single-cell Nb cavity in a large DESY furnace: (a) SE, (b) BSE.

3.3. In-situ *vacuum annealing of niobium*

In order to check our hypothesis that the contamination of the niobium surface with carbides and also oxides originated from the high-temperature phase of the treatment, a similar niobium sample was thermally annealed in UHV (950 °C/2 × 10^{-6}–2.5 × 10^{-7} Pa/11 h) in the preparation chamber of the XPS set-up. The XPS spectra ($h\nu$ = 480–1000 eV) were measured immediately after the annealing upon cooling to room temperature (without intermediate air exposure). Again, O 1*s*

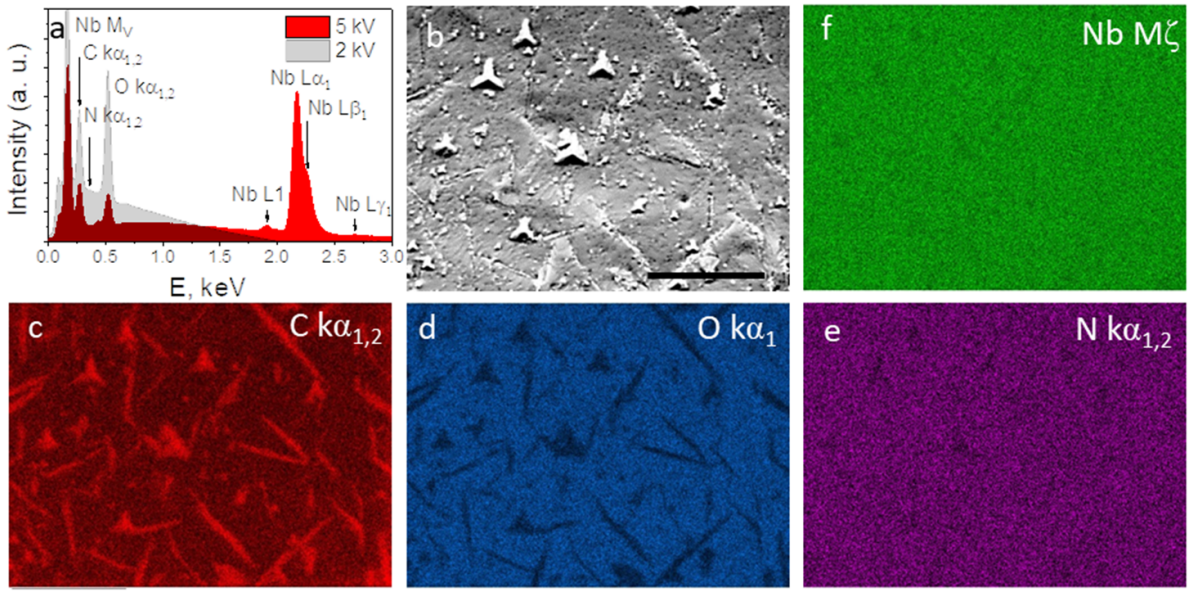

Figure 8. SEM/EDX analysis of the niobium infused without N_2 in a large DESY furnace: (a) EDX spectra collected at accelerating voltage, E_{acc}, of 5 kV and 2 kV. (b) SEM image ($E_{acc} = 2$ kV) and the corresponding EDX mapping for C (c), O (d), N (e), and Nb (f). The scale bar in figure (b) is 1 μm.

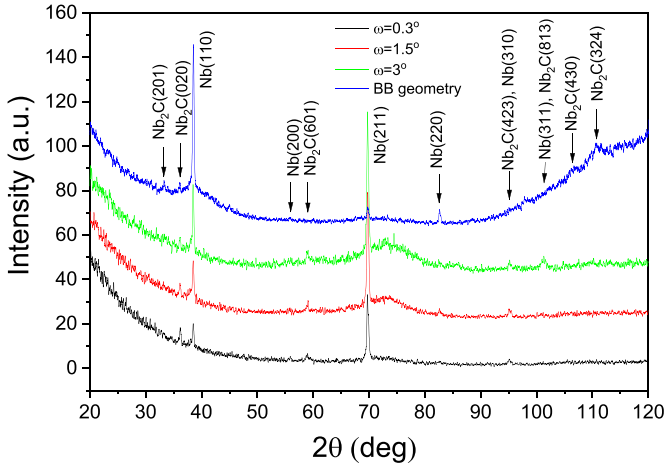

Figure 9. XRD patterns of the niobium sample infused without N_2 in the large DESY furnace together with the cavity.

from the oxygen bound to Nb with peaks at 530.2 (O^{-2}) and 531.4 eV (O^{-1}) is a feature (figure 11(a)). In addition, Nb reacted with nitrogen and carbon (figures 11(b) and (c)). N 1*s*, despite its low intensity, is complex, i.e. has at least two components at 398 eV (distinguished only at $h\nu = 480$ eV) and 397.2 eV, testifying to the formation of Nb–N and Nb–N–O bonds, respectively. The peaks at 282.5 eV and 284.0 eV within C 1*s* arising from the niobium carbide and surface adsorbates, respectively, were only detected at the lowest photon energy, therefore providing the highest surface sensitivity (the 90%-information depth is 1.8 nm at $h\nu = 480$ eV). The as-treated Nb surface appears to be free from the top pentoxide layer which significantly attenuates the photoelectron current from beneath. Higher niobium oxides present at the niobium surface in air were reduced, and the peaks corresponding to Nb^{+1} (20.6%), $Nb^{+0.4}$ (20%), Nb^0 (48.4%), were detected within Nb 3*d* (figure 11(d)). It was hardly possible to unambiguously fit the other components within the Nb-3*d* region, since the area-ratio constraint for the spin-orbital-split doublets $3d_{5/2}$ to $3d_{3/2}$ was not maintained, apparently owing to photoelectron-diffraction effects, which become more pronounced at the amorphous oxide-free single-crystal surface. Based on the analysis of N 1*s* and C 1*s*, the weak contributions from Nb–N (2.7%), Nb–N–O (5.7%) and Nb–C (2.3%) were added to Nb 3*d* at 202.72, 203.69 and 202.73 eV, respectively. To demonstrate the difference between the spectra measured *in-situ* and after exposure to air, the EDC of the Nb 3*d* collected at $h\nu = 1000$ eV is presented in the inset of figure 11(d).

For reference, a residual gas analyzer (RGA) registered approximately 6.7×10^{-8} Pa of CO, 1.0×10^{-7} Pa of CO_2 and 1.4×10^{-7} Pa of H_2O at 300 °C and total base pressure of 1.3×10^{-6} Pa, and 1.6×10^{-7} Pa of N_2, the same of CO, 1.6×10^{-8} Pa of CO_2 and 4.6×10^{-8} Pa of H_2O in the chamber at 885 °C and total base pressure of 1.9×10^{-6} Pa. At 955 °C, at the end of the anneal, only H_2O (1.3×10^{-8} Pa) and CO (2.7×10^{-8} Pa) were detected in the chamber at a total base pressure of 2.5×10^{-7} Pa (figure 3(S)).

4. Discussion

4.1. Niobium oxidation states in XPS spectra analysis

Niobium covered with the amorphous native oxide usually transforms upon vacuum annealing into a series of oxidation chemical states. Oxides with Nb valences +5, +4, +3, +2 are stable and exist as bulk phases [40]. Additionally, Nb^{+1} is commonly, but not invariably, fitted in the XPS spectra as an intermediate valence at the interface with the pure

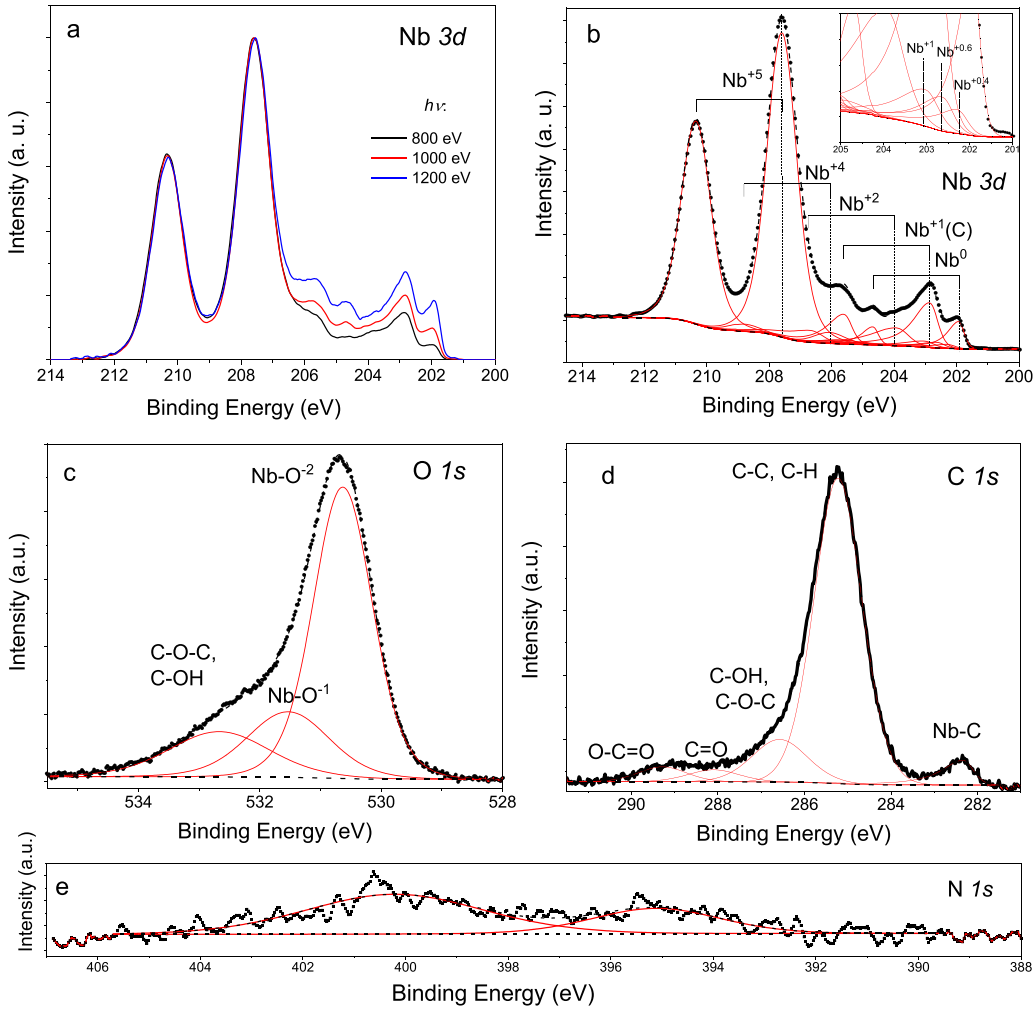

Figure 10. (a) EDCs of Nb 3*d* collected from niobium infused without N_2 together with a single-cell cavity (1DE17) at DESY as a function of incident photon energy ($h\nu = 800$, 1000 and 1200 eV). (b) An example of the fitting of the Nb 3*d* level collected at $h\nu = 1000$ eV; (c) C 1*s*, (d) O 1*s*, and (e) N 1*s*.

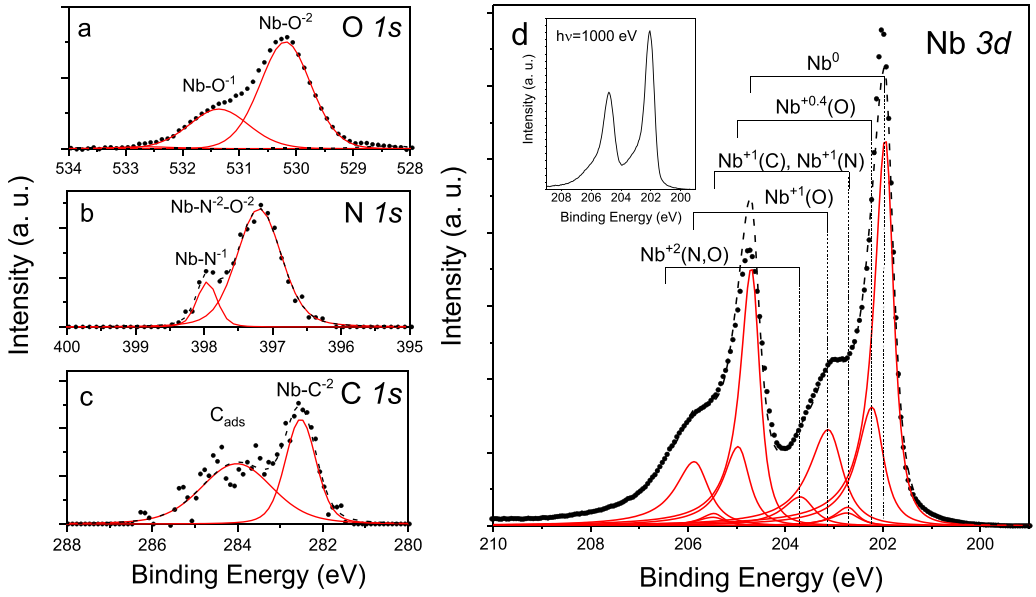

Figure 11. XPS spectra of niobium *in-situ* annealed at 950 °C ($h\nu = 480$ eV): N 1*s* (a), C 1*s* (b), and O 1*s* taken at $h\nu = 650$ eV (c), Nb 3*d* (d). In the inset of (d): Nb 3*d*, $h\nu = 1000$ eV.

Nb^0 [41]. Nb^{+3} is quite seldom fitted in the XPS spectra for such surfaces. In particular, Nb^{+3} was observed for the niobium oxidized in vacuum upon oxygen exposure [42] and via synchrotron XPS during the prolonged vacuum anneal at ∼160 °C [43].

It has been established that at $T > 598$ K in vacuum, the niobium surface consists of Nb_xO ($x \sim 1$) [28, 44] or at a prolonged anneal at 550 K, Nb_xO ($x \sim 2$) [43]. Our results on a prolonged anneal of Nb at 950 °C show that the main oxidation state at the niobium surface is Nb^{+1} which agrees with the data of Ma *et al* [43].

The EDCs of the Nb-3d core-level region of the samples treated with recipes I–III have been systematically analyzed using the fitting model employing several niobium oxidation states (Nb^{+5}, Nb^{+4}, $Nb^{+3,}$ $Nb^{+2,}$ Nb^{+1}, $Nb^{+0.6,}$ $Nb^{+0.4}$), a linear dependence of the BE shifts for niobium oxidation states in oxides and the correspondingly specified lineshapes and their FWHMs. This procedure enables quantification of the chemical states of the niobium surface after the thermal treatments under investigation. The variety of chemical species (carbon, nitrogen) present at the surface of niobium upon thermal treatments conducted in the large furnace at DESY and in the preparation chamber at RGBL has allowed the chemical shifts for niobium carbides and nitrides in such experimental conditions to be distinguished.

4.2. On the infusion treatment

Preparation of niobium cavities with nitrogen infusion has attracted a lot of interest in the SRF community around the world due to its simplicity and similarity to a standard cavity treatment utilizing low-temperature baking at 120 °C. Similarly to the standard treatment, however, the unambiguous determination of the exact mechanism causing the improvement of the cavity performance with nitrogen is challenging since the reactivity of chemical species and their diffusivities are very low at this temperature. In the present work, we analyzed with XPS the surface layer up to a depth of approximately 6.3 nm. This layer represents only a fraction of the layer that contributes to SRF losses during cold cavity operation.

During the heating and 800 °C-annealing step which is included in the treatment recipes under investigation, the native niobium oxide gradually transforms into the oxide with lower oxidation state, Nb_xO ($x = 1$–2), upon oxygen atom diffusion into the niobium bulk. In poor vacuum conditions or with sufficient surface contamination/adsorbates, chemical reactions of niobium with other elements (C, N, etc) may occur. In a standard production flow, SRF cavities after the thermal treatment are exposed to air. Therefore, the niobium samples that were either 800 °C-annealed, infused with or without N_2 were subjected to air prior to characterization. In air, niobium is readily oxidized, as confirmed by our investigation. The pentoxide formed with thickness 3–3.8 nm forms approximately 50% of the depth probed with XPS and therefore limits the information that can be extracted from the underlying material.

Concerning the nitrogen-gas interaction with niobium, adsorption and chemisorption of nitrogen take place at the clean Nb surface even at room temperature, as previously established by a volumetric technique [45]. However, upon vacuum annealing, the Nb surface is not 'clean' and presents a Nb_xO ($x = 1$–2) state, as discussed above. To the authors' best knowledge, there are no data in the literature on the absorption kinetics of N_2 with such surface in vacuum at 120 °C. It has been reported that even for small quantities of O_2 adsorbed at a clean niobium surface, no dissociative adsorption of nitrogen was detected [46]. This would mean that other adsorbates may also influence the nitrogen–niobium interaction kinetics, and therefore that the vacuum environment is critical during the infusion step. The estimated diffusion length, $2\sqrt{Dt}$, of nitrogen atoms present in the niobium lattice is roughly 0.04 nm at $D_N = 2.45 \times 10^{-23}$ cm^2 s^{-1} [47], $t = 48$ h (while for oxygen, D_O is six orders of magnitude higher) so that nitrogen could hardly have any effect on the interstitial concentration change within the surface layer. If nitrogen chemisorbed at the Nb_xO surface at 120 °C, it would influence the oxide transformation during the baking or/and niobium oxidation behavior upon subsequent exposure to air. However, no effect on the chemical state of oxygen in niobium was observed at any nitrogen flow rate used in these investigations.

Another possibility is that a nitrogen sorption layer could terminate the reaction of Nb with other species present in a vacuum chamber (CO, CO_2, etc) or, on the contrary, act as a carrier of such species. The XPS spectra of the Nb surfaces infused with and without N_2 showed only very small differences in the identified oxides and an interstitial state ($Nb^{+0.6}$) at $h\nu > 1000$ eV corresponding to larger information depths, as described in section 3.1 (figure 6). However, whether the chemical change is related to nitrogen-gas interaction with niobium during 120 °C has yet to be determined via *in-situ* infusion experiments. We suggest that, similarly to the traditional 120 °C-baking, oxygen diffusion is the key process causing most of the changes within the rf penetration depth of Nb. Indeed, the diffusion length of oxygen atoms in the Nb lattice would be ∼40 nm for the duration of the baking procedure, which is comparable to the London penetration depth for pure niobium [47]. It could therefore provide the necessary concentration of interstitials to fulfill the effects described by the theory of dirty superconductors [48].

In general, two processes take place at the surface at 120 °C: (a) drive-in diffusion of atomic species already present in the metal lattice, such as oxygen, carbon, etc, into the bulk of the metal; (b) chemisorption of atomic species, depending on the vacuum environment (partial pressure of the respective species), reactivity of species, and the chemical state of the niobium. Upon exposure to air, as discussed, it would after some days be gradually transformed into amorphous oxide [49].

As was already mentioned, the infused sample has a slightly smaller contribution from Nb^{+2} component as compared to the annealed sample. This finding agrees with the x-ray reflectivity results of [19] where the decreased thickness of NbO (Nb^{+2}) after the infusion step as compared to the 800 °C/2 h treatment was observed.

According to our data, the 120 °C-infused niobium samples, with or without N_2 supply, demonstrated slightly

larger thicknesses of the pentoxide as compared to the 800 °C-annealed Nb, which also has the highest amount of pure Nb within the same information depth. This suggests that, along with the oxygen drive-in process, oxygen incorporation (chemisorption) into niobium takes place at 120 °C-baking time and, interestingly, is not affected by the flow of N_2 at 3.3 Pa. Thus, Nb_2O_5 grows slightly thicker (∼0.3 nm) upon exposure to air at the surfaces that underwent either infusion scheme, due to the presence of excess incorporated oxygen as compared to the 800 °C-annealed niobium.

We have detected titanium contamination at the niobium infused with N_2 unlike niobium treated without N_2 gas. We assume that N_2 gas in our experimental condition acts as a carrier of heavy elements like titanium. Trace amounts of titanium were found as TiO_2 and Ti_2O_3 after exposure to air. Thus, nitrogen may facilitate the adsorption of the unwanted species from a vacuum chamber onto the niobium surface. Whether N_2 may also prevent adsorption and further interaction of other impurities with niobium needs further investigation.

An alloy of Ti and Nb could form at 800 °C (i.e. before the infusion step). Similar to interstitial impurities of C, N, O in Nb, such alloying may be associated with the hydrogen-trapping effect [50]. As for the titanium oxides, it is known that TiO_2 with rutile structure is an insulator and can substitutionally incorporate the group-V elements including Nb. Moreover, TiO_2 is known to form a complete range of solid solutions with NbO_2 [51]. If this is realized, new electronic states would be introduced into the band structure of TiO_2. Whether such local structures are present in the material under investigation and whether they influence the superconductivity properties of the Nb surface would require further investigation.

The experiment on the prolonged *in-situ* UHV anneal at 950 °C reveled nitrogen and carbon bonded to niobium at the niobium surface in the Nb^{+1}-oxidation state. We may claim that niobium interaction occurs with carbon and/or nitrogen at 800 °C in those furnaces typically characterized by a higher base pressure (10^{-4}–10^{-6} Pa). Technologically, the size, quantity and proportion of niobium carbides and nitrides (along with niobium oxides) would be affected by the residual-gas composition in the chamber, the temperature ramp during the heating stage, and the initial cleanliness of the niobium surface (proper chemical preparation and post-cleaning have to be provided to avoid acidic residue contamination). In poor vacuum conditions (with traces of O_2, CO and CO_2), the oxidation and carburation of the Nb surface would prevail (section 3.3, figures 7–11) and as a result deteriorate the superconducting properties of the niobium surface layer, since the formed phases are not superconducting at 2 K, the operation temperature of niobium cavities (T_c < 1.6 K for Nb_2C [52], 1.38 K for NbO [53]). Accordingly [17], in cavities Nb_2C cause local heating and decreasing of the reduced superconducting gap. Also, the presence of carbon in the system affects the formation of various sub-oxide phases during the thermal treatment [39] and subsequently upon air exposure due to its reduction properties. In the present work, the formation of niobium oxide in the Nb^{+2} oxidation state, corresponding to NbO which is usually characterized by a high amount of point defects in its structure and demonstrates metallic behavior in its bulk form, has been demonstrated when sufficient carbon is present in the system [40].

Comparing the infusion recipes with the standard 120 °C-recipe for cavity treatment [1, 21], the initial surface subjected to the 120 °C-bake is different: in the former, it is the Nb_2O (possibly, also NbO) with carbides and/or also nitrides, and in the latter, it is Nb_2O_5 with surface adsorbates after the air exposure, and possibly acid residue present at the surface after chemical etching. We deem that the degree of oxidation, quantity and dimension of carbides (and/or also nitrides, etc) formed at a preceding higher-temperature stage play a crucial role in whether cavity performance characteristics are improved or deteriorate and needs to be further explored *in situ*, i.e. at the Nb surface free from the native oxide.

Thus, for performing a successful cavity treatment, special attention has to be paid to the high-temperature stage (temperature ramp, residual gases in the vacuum environment, contaminant-free niobium surface) as well the equipment components (gaskets, getters) that potentially can be a source of contaminants.

5. Conclusion

In the present work, we have studied the so-called nitrogen-infusion treatment of SRF cavities with a variable-energy synchrotron XPS technique. The nitrogen-infusion treatment consists of a vacuum anneal of the cavity at 800 °C for several hours followed by a prolonged (48 h) nitrogen supply step at 120° C. Since nitrogen has low reactivity in these experimental conditions, to avoid unambiguity, the niobium surface was subjected to three different treatments: vacuum annealing at 800 °C, nitrogen infusion, and vacuum heat treatment like the infusion process but without nitrogen supply. Analysis of the core levels of niobium, nitrogen and carbon after these treatments revealed no clear evidence of nitride or carbide formation in any. Careful analysis of Nb-3*d* core level revealed only insignificant differences (within the measurement error of 1%) in the relative percentage of Nb^{+1} and $Nb^{+0.6}$ phases. The calculated thickness of the top surface layer of native oxide Nb_2O_5 appeared to be slightly larger for both infused samples (∼3.8 nm) as compared to the annealed one (∼3.5 nm), which implies insignificant oxygen incorporation into niobium during the 120 °C bake and that the flow of nitrogen has no effect on the formation of the oxide phases. It was found that nitrogen gas supplied during the infusion may promote the deposition of titanium oxide at the niobium surface if titanium components are present in the furnace. Additionally, the analysis of the niobium after an unsuccessful infusion (as proven by cavity SRF tests) confirmed the formation of a carbide phase Nb_2C as well as an increased amount of Nb^{+2} (NbO) but also depletion of Nb^{+5} (Nb_2O_5) and $Nb^{+0.4}$ (interstices). Furthermore, by conducting a prolonged (11 h) *in-situ* annealing of niobium at 950 °C in the preparation chamber of the XPS set-up, we proved that the formation of undesired Nb–N and Nb–C phases occurs even in UHV conditions. Thus, we have demonstrated that vacuum-furnace hygiene, particularly

during the high-temperature stage of the vacuum treatment, is a prerequisite for the success and reproducibility of nitrogen infusion or similar thermal treatments.

Data availability statement

All data that support the findings of this study are included within the article (and any supplementary files).

Acknowledgments

We express special thanks to X Singer and W Singer for providing raw niobium material for the present investigation. DESY M-group members particularly A Matheisen, B van der Horst, W-D Möller, M Schmökel, N Steinhau-Kuehl, D Reschke, M Wenskat, and N Walker are particularly acknowledged for organising and performing the thermal annealing of a niobium sample together with the SRF cavity. A Stierle and S Kulkarni (DESY Nanolab) and F Ruske (HZB) are acknowledged for the assistance in SEM/EDX measurements. We acknowledge the opportunity to perform measurements at the facilities of the X-Ray CoreLab (HZB) supervised by A Ramírez Caro. The contribution of O M and V A was supported by the RFBR (Grant No. 20-02-00489). BMBF Project SRF_RandD and InnovEEA (01.01.2020-31.12.2023) Project are acknowledged for the financial support.

ORCID iDs

A Prudnikava https://orcid.org/0000-0003-0647-2546
Y Tamashevich https://orcid.org/0000-0003-0608-6485
S Babenkov https://orcid.org/0000-0001-6996-4084
A Makarova https://orcid.org/0000-0002-5603-5566
V Aristov https://orcid.org/0000-0002-9596-9898
O Molodtsova https://orcid.org/0000-0001-6321-758X
O Kugeler https://orcid.org/0000-0003-0157-2118
J Viefhaus https://orcid.org/0000-0003-1154-0750
B Foster https://orcid.org/0000-0001-5699-3046

References

[1] Visentin B, Charrier J, Coadou B and Roudier D 1999 *9th Workshop on RF Superconductivity* (*Santa Fe, NM, USA*) p 198
[2] Ciovati G, Kneisel P and Gurevich A 2007 *Phys. Rev. Accel. Beams* **10** 062002
[3] Ciovati G, Myneni G, Stevie F, Maheshwari P and Griffis D 2010 *Phys. Rev. Accel. Beams* **13** 022002
[4] Romanenko A and Padamsee H 2010 *Supercond. Sci. Technol.* **23** 045008
[5] Visentin B, Barthe M, Moineau V and Desgardin P 2010 *Phys. Rev. Accel. Beams* **13** 052002
[6] Romanenko A, Grassellino A, Barkov F and Ozelis J 2013 *Phys. Rev. Accel. Beams* **16** 012001
[7] Ma Q and Rosenberg R A 2003 *Appl. Surf. Sci.* **206** 209–17
[8] Delheusy M, Stierle A, Kasper N, Kurta R, Vlad A, Dosch H, Antoine C, Resta A, Lundgren E and Andersen J 2008 *Appl. Phys. Lett.* **92** 101911
[9] Ciovati G 2006 *Appl. Phys. Lett.* **89** 022507
[10] Grassellino A, Romanenko A, Sergatskov D, Melnychuk O, Trenikhina Y, Crawford A, Rowe A, Wong M, Khabiboulline T and Barkov F 2013 *Supercond. Sci. Technol.* **26** 102001
[11] Yang Z, Lu X, Tan W, Zhao J, Yang D, Yang Y, He Y and Zhou K 2018 *Appl. Surf. Sci.* **439** 1119–26
[12] Grassellino A, Romanenko A, Trenikhina Y, Checchin M, Martinello M, Melnychuk O, Chandrasekaran S, Sergatskov D, Posen S and Crawford A 2017 *Supercond. Sci. Technol.* **30** 094004
[13] Dhakal P, Ciovati G, Pudasaini U, Chetri S, Balachandran S and Lee P J 2019 *Phys. Rev. Accel. Beams* **22** 122002
[14] Veit R D, Farber R G, Sitaraman N S, Arias T A and Sibener S 2020 *J. Chem. Phys.* **152** 214703
[15] Umemori K, Kako E, Konomi T, Michizono S, Sakai H, Tamura J and Okada T 2019 *Proc. Int. Conf. SRF* pp 499–502
[16] Wenskat M, Prudnikava A, Reschke D and Schaffran J 2017 *Proc. Int. Conf. SRF* pp 759–61
[17] Wenskat M, Bate C, Pandey A D, Jeromin A, Keller T F, Knobloch J, Köszegi J, Kramer F, Kugeler O and Kulkarni S 2020 *Supercond. Sci. Technol.* **33** 115017
[18] Dhakal P, Chetri S, Balachandran S, Lee P J and Ciovati G 2018 *Phys. Rev. Accel. Beams* **21** 032001
[19] Semione G, Pandey A D, Tober S, Pfrommer J, Poulain A, Drnec J, Schütz G, Keller T, Noei H and Vonk V 2019 *Phys. Rev. Accel. Beams* **22** 103102
[20] Powell C J and Jablonski A 2010 *J. Electron Spectrosc.* **178** 331–46
[21] DESY D E S 2009 Series surface and acceptance test preparation of superconducting cavities for the European XFEL XFEL/A-D, Revision B
[22] Fedoseenko S, Vyalikh D, Iossifov I, Follath R, Gorovikov S, Püttner R, Schmidt J-S, Molodtsov S, Adamchuk V and Gudat W 2003 *Nucl. Instrum. Methods Phys. Res.* A **505** 718–28
[23] Viefhaus J, Scholz F, Deinert S, Glaser L, Ilchen M, Seltmann J, Walter P and Siewert F 2013 *Nucl. Instrum. Methods Phys. Res.* A **710** 151–4
[24] Babenkov S V, Aristov V Y, Molodtsova O V, Winkler K, Glaser L, Shevchuk I, Scholz F, Seltmann J and Viefhaus J 2015 *Nucl. Instrum. Methods Phys. Res.* A **777** 189–93
[25] Engelhard M H, Baer D R, Herrera-Gomez A and Sherwood P M 2020 *J. Vac. Sci. Technol.* A **38** 063203
[26] Rumble J J, Bickham D and Powell C 1992 *Surf. Interface Anal.* **19** 241–6
[27] Bahl M 1975 *J. Phys. Chem. Solids* **36** 485–91
[28] King B, Patel H, Gulino D and Tatarchuk B 1990 *Thin Solid Films* **192** 351–69
[29] Walton J, Wincott P, Fairley N and Carrick A 2010 *Peak Fitting with CasaXPS: A Casa Pocket Book* (Knutsford: Accolyte Science)
[30] Major G H, Avval T G, Patel D I, Shah D, Roychowdhury T, Barlow A J, Pigram P J, Greiner M, Fernandez V and Herrera-Gomez A 2021 *Surf. Interface Anal.* **53** 689–707
[31] Dupin J-C, Gonbeau D, Vinatier P and Levasseur A 2000 *Phys. Chem. Chem. Phys.* **2** 1319–24
[32] Beamson G and Briggs D 1992 *Mol. Phys.* **76** 919–36
[33] Gries W H 1996 *Surf. Interface Anal.* **24** 38–50
[34] Carlson T A and McGuire G 1972 *J. Electron Spectrosc. Relat. Phenom.* **1** 161–8
[35] Strohmeier B R 1990 *Surf. Interface Anal.* **15** 51–56
[36] Jablonski A and Powell C 1993 *Surf. Interface Anal.* **20** 771–86
[37] Tanuma S, Powell C and Penn D 2011 *Surf. Interface Anal.* **43** 689–713
[38] Vishwanadh B, Murthy T C, Arya A, Tewari R and Dey G 2016 *J. Alloy. Compd.* **671** 424–34
[39] Ono K 1993 *High Temp. Mater. Process.* **11** 207–16

[40] Nico C, Monteiro T and Graça M P 2016 *Prog. Mater. Sci.* **80** 1–37
[41] Alov N 2005 *J. Anal. Chem.* **60** 431–5
[42] Thiam M M and Bastl Z 2002 *Surf. Sci.* **507** 678–82
[43] Ma Q, Ryan P, Freeland J and Rosenberg R 2004 *J. Appl. Phys.* **96** 7675–80
[44] Delheusy M 2008 *Doctoral Thesis Universite Paris-Sud XI* University of Stuttgart p 188
[45] Pasternak R and Gibson R 1965 *Acta Metall. Mater.* **13** 1031–8
[46] Fromm E and Mayer O 1978 *Surf. Sci.* **74** 259–75
[47] Mehrer H 2007 *Diffusion in Solids: Fundamentals, Methods, Materials, Diffusion-controlled Processes* (Berlin: Springer) (https://doi.org/10.1007/978-3-540-71488-0)
[48] Anderson P W 1959 *J. Phys. Chem. Solids* **11** 26–30
[49] Grundner M and Halbritter J 1984 *Surf. Sci.* **136** 144–54
[50] Shirley A and Hall C 1986 *In Perspectives in Hydrogen in Metals* (Amsterdam: Elsevier) pp 395–402
[51] Morris D, Dou Y, Rebane J, Mitchell C, Egdell R, Law D, Vittadini A and Casarin M 2000 *Phys. Rev.* B **61** 13445
[52] Roberts B W 1972 *Properties of Selected Superconductive Materials* (New York: US Department of Commerce, National Bureau of Standards)
[53] Hulm J, Jones C, Hein R and Gibson J 1972 *J. Low Temp. Phys.* **7** 291–307